Microstructural Evolution during Laser Resolidification of Fe-18 At. Pct Ge Alloy

KRISHANU BISWAS and KAMANIO CHATTOPADHYAY

The technique of laser resolidification has been used to study the rapid solidification behavior of concentrated Fe-18 at. pct Ge alloy. The microstructural evolution has been studied as a function of scanning rate of laser beam. Scanning electron microscopy (SEM) reveals the formation of a two-layer (designated as "A" and "B") microstructure in the remelted pool. The A layer shows a band consisting of a network of interconnected channels and walls, quite similar to cell walls. The B layer shows dendritic growth. Transmission electron microscopic observations reveal the formation of bcc α-FeGe in the B layer. Laser melting has been found to play an important role in formation of the A layer. Microstructural evolution in B has been analyzed using the competitive growth criterion, and formation of bcc α-FeGe has been rationalized in the remelted layers.

DOI: 10.1007/s11661-009-0084-y

I. INTRODUCTION

ALTHOUGH research on rapid solidification of dilute alloys is well known in the literature,[1–10] the study of microstructural evolution during rapid resolidification of concentrated alloys is scarce and has been less understood in terms of experiments as well as theory.[2–4] The phase selection and development of the morphology of the advancing solid-liquid interface of concentrated alloy systems is a field that remains to be explored. The technique of laser resolidification allows us to study the solidification behavior of these alloys under controlled growth conditions. It involves rapid melting and solidification of a thin layer on the surface of a sample (pure metal or alloy) by traversing a high power laser beam at a certain scanning speed. This process involves solidification at high rates (as high as 18 ms^{-1}[3]) depending on the laser power, scanning speed, type of material, *etc*. Therefore, the conditions of equilibrium can no longer be assumed at the advancing solid/liquid interface, and thus, formation of metastable phases and microstructures are possible.[3]

It has been reported in References 2, 6, 7, 10, and 11 that the microstructural evolution during laser resolidification is strongly influenced by the growth kinetics and thermal history of the alloy pool. During this process, the molten pool created by the laser beam remains in contact with the underlying solid alloy. Therefore, the microstructural evolution can be considered as purely growth phenomenon. The growth velocity of the solid/liquid interface can be measured directly from the as-solidified microstructure[2,11] and related to the corresponding microstructure. However, it is not possible to experimentally measure the temperature gradient inside the remelted pool. However, we can obtain an estimate of the temperature gradients using the heat-transfer models.[9,10,12,13] These numerical calculations allow us to obtain the temperature distribution in the laser-remelted region by solving the continuity, momentum, and enthalpy conservation equations with respect to a reference frame fixed to the laser beam.[12] In fact, the intimate contact of the surface-melted layer and the underlying solid makes it reasonable to compare the experimental results with numerical calculations.

The primary aim of the present study is to understand the evolution of the microstructure during laser resolidification of a concentrated Fe-Ge alloy containing 18 at. pct Ge. Figure 1(a) shows the Fe-rich part of the Fe-Ge phase diagram.[14] Under equilibrium conditions, the solidification of Fe-18 at. pct Ge alloy starts with the nucleation of bcc α-FeGe phase (a = 0.288 nm). The α phase undergoes two ordering transitions upon further cooling in solid state: $\alpha \rightarrow \alpha_2$ (B2, a = 0.288 nm) at 1230 °C (1503 K) and $\alpha_2 \rightarrow \alpha_1$ phase (DO_3, a = 0.576 nm) at 900 °C (1173 K). The motivation of the present investigation originates from our work on undercooling of Fe-18 at. pct Ge alloy using electromagnetic levitation.[15] We attempt to rationalize the experimental observations in terms of phase transformation under nonequilibrium conditions during laser melting followed by the process of rapid solidification. It will be shown that melting of the concentrated alloy during laser beam interaction at high speed has a very important role in microstructural evolution.[16,17]

II. EXPERIMENTAL DETAILS

Fe-Ge alloys containing 18 at. pct Ge were prepared by arc melting of high-purity iron (99.9 pct purity) and

KRISHANU BISWAS, Assistant Professor, is with the Department of Materials and Metallurgical Engineering, Indian Institute of Technology, Kanpur, U.P. - 208016, India. Contact e-mail: kbiswas@iitk.ac.in KAMANIO CHATTOPADHYAY, Professor, is with the Department of Materials Engineering, Indian Institute of Science, Bangalore - 560 012, India.

Manuscript submitted April 26, 2009.
Article published online December 22, 2009

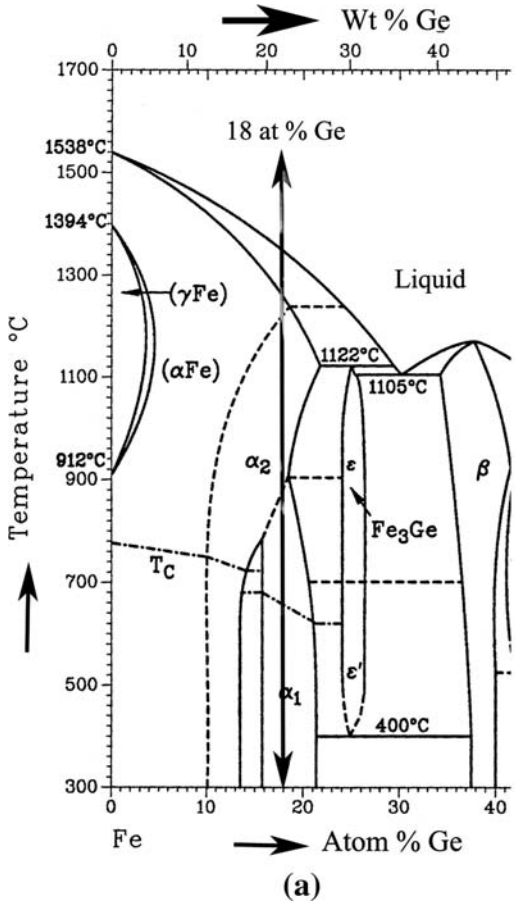

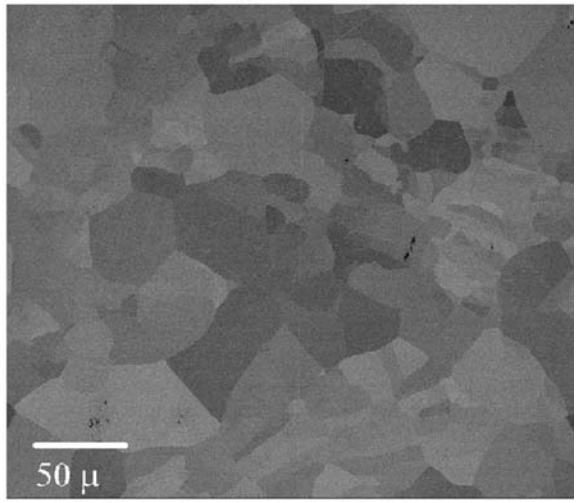

Fig. 1—(*a*) Fe-rich part of Fe-Ge phase diagram[14] and (*b*) low-magnification SEM image of as-cast alloy. The red arrow in (a) denotes the composition of alloy under study.

Table I. Experimental Parameters Used in the Present Study

Power Density (W/m^2)	Interaction Time (s)	Traverse Speed V_b (m/s)	Depth, D (μm) (from Microstructure)	Width, W (μm) (from Microstructure)
1.7×10^1	3×10^{-2}	5×10^{-2}	150 ± 5	1360 ± 12
1.7×10^1	5×10^{-3}	16.7×10^{-2}	115 ± 5	848 ± 10
1.7×10^1	2×10^{-3}	25×10^{-2}	48 ± 4	545 ± 10

germanium (99.999 pct purity). The samples were melted repeatedly in order to remove any compositional inhomogeneity. Rapid solidification experiments were carried out using a continuous wave 10 kW CO_2 laser (Rofin Sinar, RS10000, Plymouth, MI). The surface on which laser treatment to be performed was polished flat. Prior to the laser treatment, all the samples were ground on 100 grit SiC emery paper to ensure similar surface quality and to enhance the absorption of the laser beam. In order to refine inhomogeneous as-cast microstructure, all specimens underwent double laser treatments. In the first case, the sample surface was scanned by overlapping laser traces over the entire surface at relatively moderate laser power density of 1.2×10^4 W/cm^2 and an interaction time of 10^{-2} seconds. These ensure compositional homogeneity over a large depth (~200 to 300 μm). Several experiments were performed prior to final resolidification experiment on this alloy. Initial trials were done using different powers and scanning speeds to obtain a stable melt pool. Melting of single traces was carried out with 3 kW laser power and different scanning speeds (V_b). The details of the parameters used in the laser treatment are listed in Table I. During the laser treatment, a continuous flow of argon gas (8 L/min) was maintained to prevent oxidation of the molten pool.

Microstructural analysis of the as-cast as well as resolidified layers was carried out using scanning electron microscopy (SEM, FEI make Sirion operating at 20 kV, Eindhoven, The Netherlands). The chemical analyses were

performed using a Cameca (Paris, France) SX100 electron probe microanalyzer (EPMA) operating at 30 kV and 40 nA. The fine scale microstructure and phase analysis was carried out using a transmission electron microscope (JEOL* 2000 FXII) operating at 200 kV.

*JEOL is a trademark of Japan Electron Optics Ltd., Tokyo.

In Section III, the microstructure of the as-cast specimen will be presented first. This will be followed by the results of the samples processed at low (5×10^{-2} m/s), moderate (16.7×10^{-2} m/s), and high (25×10^{-2} m/s) scanning speeds.

III. RESULTS

A. *As-Cast Microstructure*

The scanning electron micrograph of a representative as-cast sample, which has been used for resolidification experiments, is shown in Figure 1(b). The microstructure reveals large grains (20 to 80 μm) of single-phase material. The compositional analysis using an EPMA shows a mean composition of Fe-18 at. pct Ge with a scatter of ±0.2 at. pct. The transmission electron microscopic studies (not shown here) indicate the presence of DO_3 ordering in the sample.

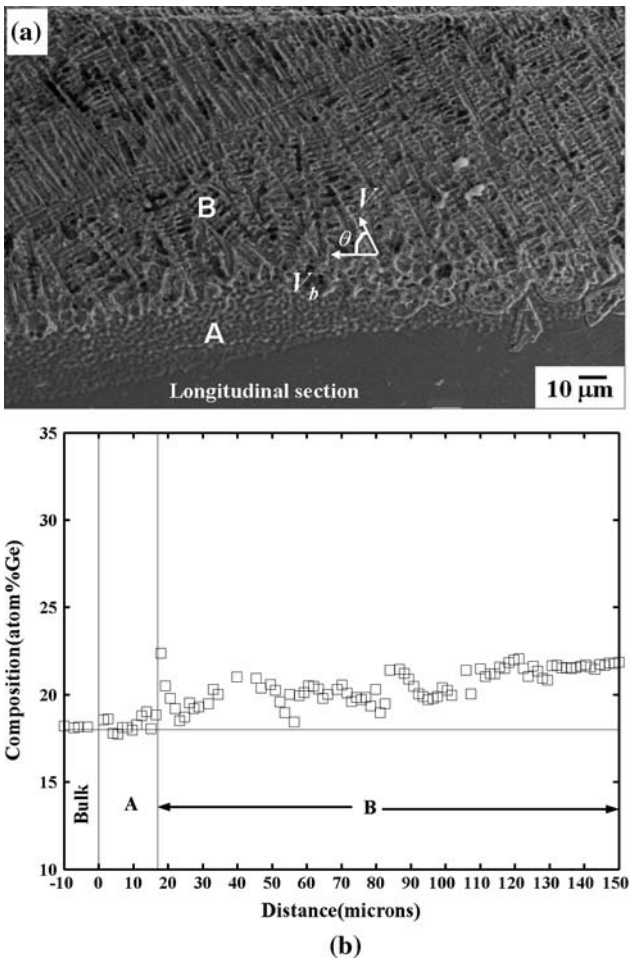

Fig. 2—(*a*) Low-magnification SEM image of the longitudinal section of the sample resolidified at 5 cm/s and (*b*) compositional measurement along the height of the remelted layer measured by an EPMA.

B. *Sample Processed by Laser Scanning Speed of 5×10^{-2} m/s*

The SEM observations of the sample laser resolidified at a scanning rate of 5×10^{-2} m/s. are presented in Figures 2 and 3. Figure 2(a) is a low-magnification SEM micrograph of the longitudinal section of the resolidified layer. The depth of the resolidified layer is about 150 μm. The growth direction (V_s) and laser beam scanning directions (V_b) are marked on the micrograph. By calculating the local angle (θ) between V_s and V_b, one can calculate the local solidification velocity according to the following relationship:[2]

$$V_S = V_b \cos\theta \qquad [1]$$

The microstructural studies reveal formation of two separate layers marked as A and B in Figure 2(a). Layer A shows a band of small dark specks adjacent to the interface. The thickness of this band is about 25 μm. Layer B (125 μm) reveals the typical dendritic growth morphology. The compositional analysis of the remelted layer has been carried out using an EPMA. Figure 2(b) shows the composition profile along the height of the remelted layer. The germanium content in layer A is almost the same as that of the bulk of the sample. However, layer B shows enrichment of solute (19 to 22 at. pct Ge). The germanium concentration increases from the bottom to the top of the layer with minor fluctuations at different locations. The top portion of layer B (~40 μm) shows no fluctuations in composition. It is evident that the measurement of angle θ from the microstructural features in the A layer is not possible, because the microstructural features are not properly aligned in this layer as compared to layer B.

To understand the characteristics of the layers with different microstructure, the high-magnification secondary electron (SE) and backscattered electron (BSE) micrographs of the transverse section of the remelted layer are presented in Figures 3(a) and (b). The two layers (A and B) are marked on the micrographs. Layer A shows the cell-like growth morphology, whereas layer B reveals dendritic morphology, which covers the rest of the remelted layer. The inset in Figure 3(a) shows the blown-up view of layer A. It shows a fine network of interconnected channels and walls, quite similar to cell walls. Similar growth morphologies are also observed in Figure 3(b), which is a BSE image of the same region. The black lines on the image indicate the lines along which compositional measurements are carried out using an EDS attached to a scanning electron microscope.

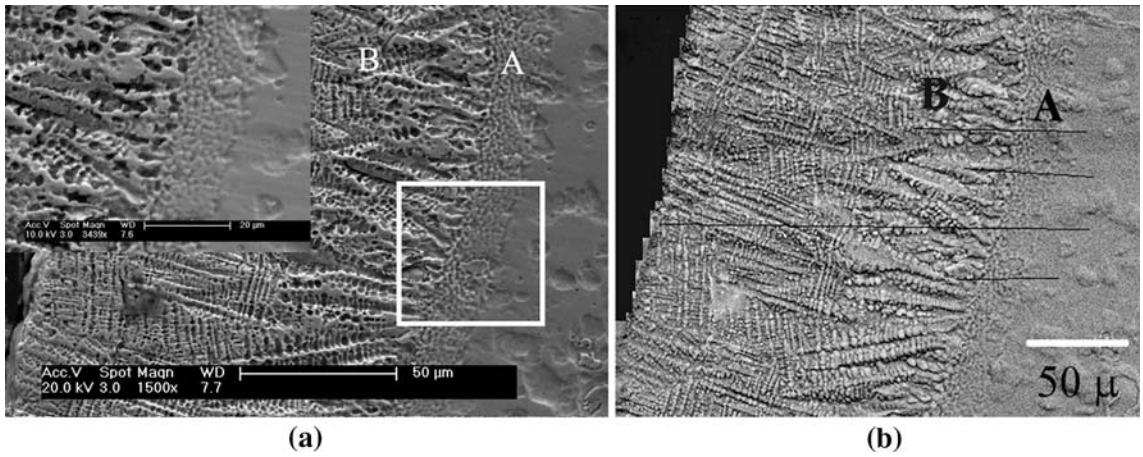

Fig. 3—(*a*) High-magnification SE image of the sample resolidified at 5×10^{-2} m/s with the inset showing a blown-up view of the region near the bottom of the remelted layer and (*b*) high-magnification BSE image. The black lines in (b) indicate EDS measurements.

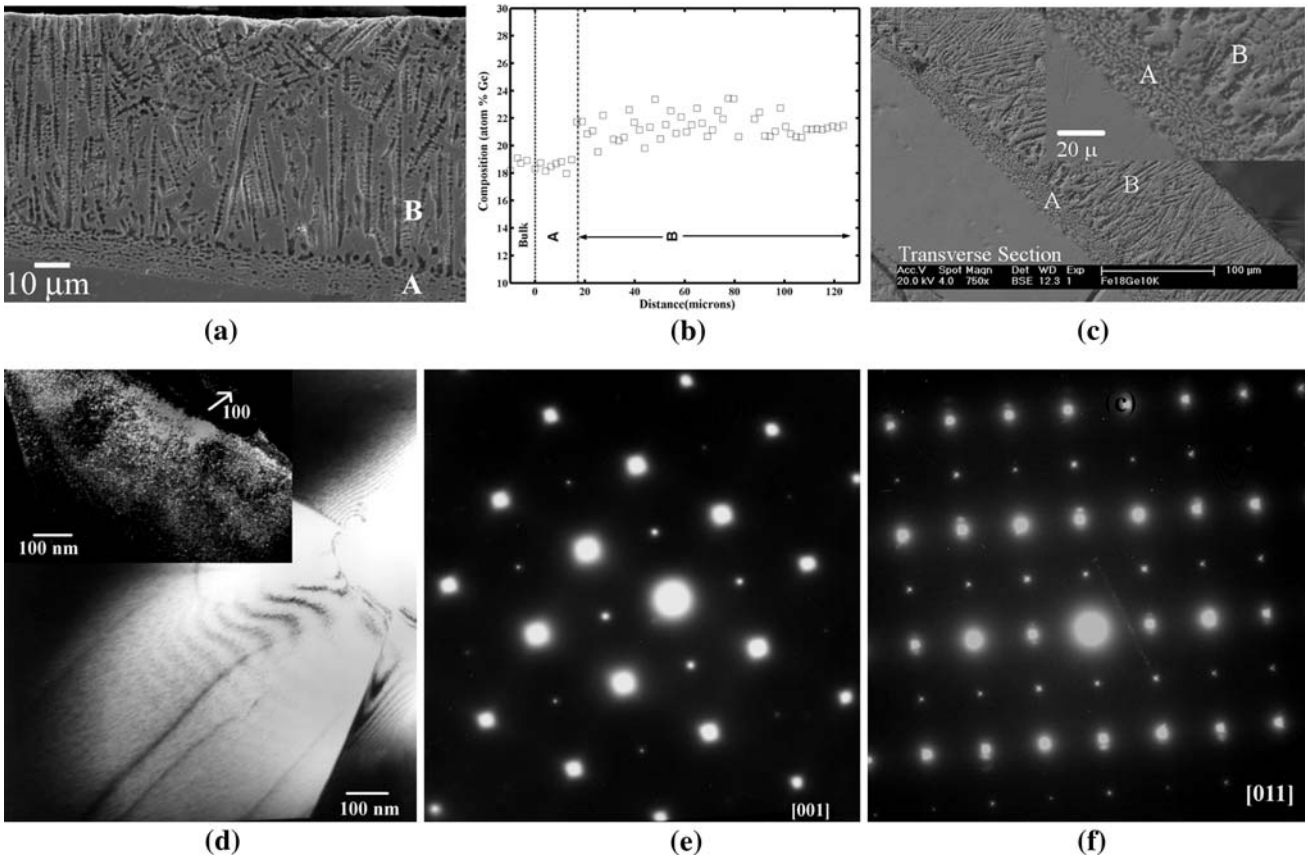

Fig. 4—(*a*) Low-magnification image of the transverse section of the sample resolidified at 16.7×10^{-2} m/s, (*b*) compositional measurements along the height of the remelted layer measured by an EPMA, (*c*) high-magnification BSE image of the same region with an inset showing the blown-up view of the region near the bottom of the remelted layer, and (*d*) TEM bright-field micrograph showing grains in layer B. (*e*) [001] zone axis and (*f*) [011] zone axis patterns revealing B2 ordering. The inset on (d) shows (100) dark-field micrograph lighting up fine scale B2 domains.

C. *Sample Processed by Laser Scanning Speed of 16.7×10^{-2} m/s*

The microstructural investigation of the resolidified sample obtained by laser processing at 16.7×10^{-2} m/s is shown in Figure 4. The low-magnification SEM images of the transverse section of the remelted layer are presented in Figure 4(a). The thickness of the latter is about 125 μm. The remelted layer shows similar

microstructural characteristics as that of the sample that was processed at a laser scanning speed of 5×10^{-2} m/s. Two microstructural layers are marked as A (15 μm) and B (110 μm) in the micrograph. The results of the compositional measurements of the remelted layer as performed using an EPMA are shown in Figure 4(b). Layer B is substantially enriched with solute (20 to 24 at. pct Ge), whereas the composition of layer A is the same as that of the bulk of the alloy. One can also observe compositional fluctuations in layer B. High-magnification SEM micrographs as shown in Figure 4(c) reveal similar growth morphologies as presented in Figure 3(a), illustrating two microstructural layers.

Figure 4(d) summarizes the transmission electron microscopy (TEM) observations. The low-magnification bright-field micrograph of layer B indicates that the single-phase microstructure consists of grains of 0.5 μm. Selected area diffraction (SAD) patterns along different crystallographic zone axes are obtained from one such grain. Figures 4(e) and (f) show SAD patterns along the [001] and [011] directions. The analysis of the pattern indicates the presence of B2 ordering in the grains. Analysis of the SAD pattern along the [011] directions shows the absence of the {111} type of spots, indicating the absence of DO_3 ordering. The dark-field micrograph obtained using (100) reflection is shown as an inset in the figure. The presence of fine scale B2 domains is clearly visible in the micrograph.

D. *Sample Processed by Laser Scanning Speed of 25 × 10^{-2} m/s*

Figure 5 shows the microstructure of the resolidified region of the sample processed with a scanning speed of 25×10^{-2} m/s. Figure 5(a) reveals the low-magnification SEM image of the 50-μm-thick remelted layer. The high-magnification BSE image of the remelted layer is shown as the inset in Figure 5(a). It is evident that the microstructure in the remelted layer also consists of two separate layers, A and B, as observed in previous cases. The thicknesses of the layers are about 8 and 40 μm, respectively. The detailed analysis of the microstructure reveals that the microstructural features are the same as discussed earlier. Figure 5(b) presents the compositional measurements made along the height of the remelted layer using an EPMA. The compositional analysis indicates that the Ge concentration in the A layer does not differ much from the alloy composition. The B layer has a higher Ge concentration (20 to 26 at. pct Ge).

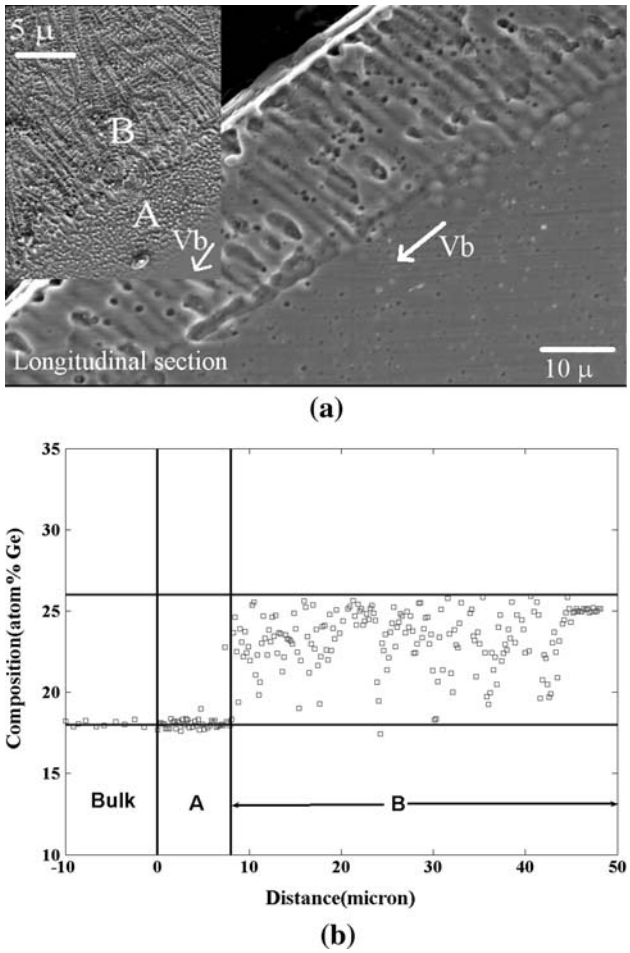

Fig. 5—(*a*) Low-magnification image of the transverse section of the sample resolidified at 25×10^{-2} m/s, and (*b*) compositional measurements along the height of the remelted layer measured by an EPMA. The inset on (a) shows the high-magnification image of the region near the interface between the resolidified region and unaffected sample.

IV. DISCUSSION

A. *Microstructural Evolution of the Remelted Layer*

It is evident that the microstructure in the remelted region of the samples processed with different scanning speeds consists of two layers: A and B. The microstructural evolution in the remelted layer is independent of the scanning speed of the laser beam. The thickness of the layers varies as a function of scanning speeds. In this section, we shall discuss the formation of two microstructural layers (A and B) in the remelted regions separately.

The formation of layer A in the resolidified samples can be explained invoking the concept developed by Allen *et al.*[16] that the microstructure developed in A is the consequence of rapid laser melting prior to the rapid solidification of the molten liquid.[16,17] Melting has indeed been found to play a key role in the evolution of the final microstructure of pure metals and alloys.[16] The melting of an alloy is different from that of a pure metal. It is always accompanied by the redistribution of solutes between the solid and liquid phases. For concentrated alloys, this redistribution requires a very slow rate of melting at equilibrium. In addition, although superheating of pure metals is difficult to attain, relatively high levels of superheating can be achieved in alloys under non-steady-state conditions, such as at sufficiently high rates of heating, using a laser beam.[16] The loss of equilibrium can occur at the advancing liquid/solid interface of a concentrated alloy at relatively slow interface velocities as compared to the higher rates of melting required for a pure metal.

This usually happens when a driving force for melting is solutal,[17] which is the case for concentrated alloys.

We now discuss the present case as a laser beam heats the solid. We assume the solid to be in local equilibrium with the liquid. After reaching the solidus temperature, T_s (1250 °C (1523 K) for the present alloy), during laser heating, the melting of the solid begins at the surface of the sample because there is no (or infinitesimally small) nucleation barrier for melting at the free surface.[17] At a temperature, T, slightly above T_s, there will be a liquid layer of composition C_0/k (~22.86 at. pct Ge) formed at the surface, where C_0 is the alloy composition (18 at. pct Ge) and k the partition coefficient. Thereafter, melting would only require the growth of this liquid layer inward during subsequent laser heating. To observe melting under equilibrium conditions, the heating rate must be maintained too low to allow complete partition of solute between the solid and liquid for this concentrated alloy. As the heating rate is increased, there will be an associated decrease in time for diffusion. This will cause development of a compositional gradient within the solid ahead of the melting front. Eventually, this will lead to retaining a solid of original composition (C_0) at temperature above T_s. Therefore, part of the solid ahead of the melting front will demonstrate some level of constitutional superheating as the heating rate is increased. This effect will be stronger as the heating rate increases.

The heating rate during laser processing cannot be measured experimentally. However, numerical calculation using heat-transfer models allows us to calculate the temperature at any point inside the remelted pool as a function of time. We adopted a numerical model described previously by Sarkar *et al.*[12] This model addresses melting and subsequent solidification taking into account the fluid flow in the molten pool. The model parameters are fine tuned for the case of scanning speed of 5×10^{-2} m/s and, subsequently, the same parameters used for other cases consistent with

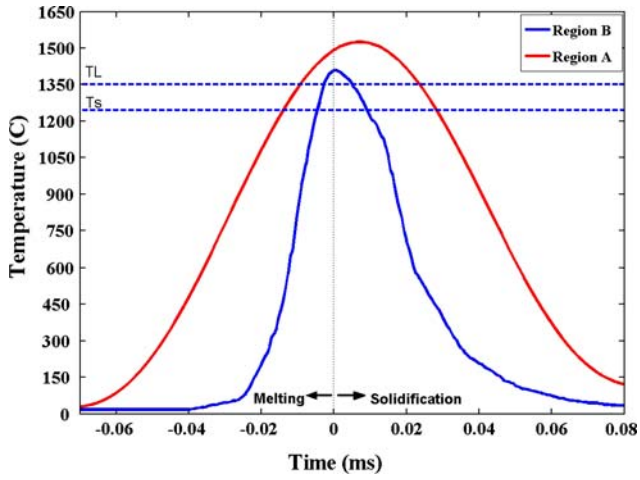

Fig. 6—Calculated thermal history of the two points corresponding to regions A and B in the remelted layer. Melting and solidification cycles are indicated in the figure. T_s and T_l correspond to solidus and liquidus temperatures of the alloy, respectively.

experiments. The typical temperature history at two locations corresponding to regions A and B for the sample processed with scanning speed of 5×10^{-2} m/s is shown in Figure 6. The melting and solidification cycles are indicated in the figure. The slope of these curves represents the prevailing heating/cooling rates existing in the solid and liquid during laser processing. It can be seen that, irrespective of the melting temperature, the heating rate is sufficiently high (10^5 K/s) for deviation from equilibrium to occur. Therefore, it is highly likely that the solid ahead of the melting front will exhibit some level of constitutional superheating.

However, the development of such a constitutionally superheated solid during laser heating will also depend on the melting rate of the solid, because constitutional superheating requires the development of compositional gradient in the solid ahead of the melting front. This requires establishment of a viable diffusional profile across the melting front. Unlike the solidification velocity, it is not possible to experimentally measure the local melting rate during laser processing. In such a case, we have made an attempt to calculate the average melting rate (R_m) using the following approach. The shape of the melt pool generated by the laser beam at any particular position is found to be hemispherical.[11] If the effective diameter of the melt pool is d_{eff}, the longest perimeter (L) in the melt pool is equal to the melt/substrate interface. The shortest perimeter of the melt pool is d_{eff}. Therefore, the average melting rate is given by

$$R_m = \frac{(\pi d_{\text{eff}} + d_{\text{eff}})/2}{t_{\text{int}}} \qquad [2]$$

where t_{int} is the interaction time (t_{int} is the time the laser beam stays at a particular position on the sample surface). During the laser remelting process at a fixed laser power and constant scanning speed, a steady-state pool is created. Therefore, d_{eff} will be the same as the beam diameter under steady-state conditions. The melt pool interaction time depends on the values of d_{eff} and scanning speed (V_b), $t_{\text{int}} = \frac{d_{\text{eff}}}{V_b}$, all other factors being constant.

At a high speed of remelting, the width of laser tracks has been found to be identical with the beam diameter. The relevant laser parameters are listed in Table I. Using such an approach yields $R_m = 9.4 \times 10^{-2}$ m/s for $V_b = 5 \times 10^{-2}$ m/s, whereas $R_m = 35.1 \times 10^{-2}$ m/s for $V_b = 16.7 \times 10^{-2}$ m/s and $R_m = 56.4 \times 10^{-2}$ m/s for $V_b = 25 \times 10^{-2}$ m/s. The average melting rate must be compared with the solvent diffusion speed in order to obtain any conclusion about superheating. We now calculate the diffusional speed of the solvent (species rejected into the solid during melting, Fe) using the formula given by Aziz.[18] The diffusivity of iron in the Fe-18 at. pct Ge alloy in the temperature range close to the solidus temperature is not available in the literature. The diffusivity of iron in homogeneous Fe-4 at. pct Ge alloy is reported in the literature[19] in the temperature range of 900 °C to 1200 °C. To a first approximation, we can use $D_s = 1.43 \times 10^{-12}$ m^2/s at 1200 °C, which is close to the solidus temperature (1250 °C) of the present

alloy composition in our calculations. Dividing D_s by the characteristic solid/liquid interface thickness of a few atomic distances ($\delta = 10^{-9}$ cm) yields a diffusional velocity of solvent of 0.143×10^{-2} m/s, which is two orders of magnitude lower than the R_m obtained for all scanning velocities. Therefore, no viable diffusional profile could be established into the solid at the melting rates calculated during our experiments. Thus, the solid would not be "constitutionally" but "thermally" superheated during rapid laser heating. The melting of the superheated solid can then take place at any temperature above T_s *via* internal nucleation of the liquid ahead of the melting front.

The structural perfection of the high-purity alloy may allow achievement of higher superheating levels for a given heating rate by minimizing the number of active internal sites within the sample. Under certain conditions, the heating rate (~10^4 K/s in the present case) can be sufficiently high so that the maximum temperature reached prior to melting of the superheated solid will be T_0.[16] At T_0, the two phases, solid and liquid having the same composition, will have the same free energy. Thus, T_0 represents the limit of partitionless transformation. In the present investigation, the determination of T_0 requires free energy expressions of the solid and liquid phases of the alloys. The free energy expression for the liquid phase of $Fe_{100-x}Ge_x$ ($0 \le x \le 24$) has been estimated by Kanibolorsky *et al.*[20] For the solid, we have used the free energy expressions obtained by Inden *et al.*[21] Figure 7 shows the Fe-rich portion of the Fe-Ge phase diagram with the calculated T_0 curve. The solidus and liquidus of α-FeGe are drawn as solid curves and the calculated T_0 curve is indicated on the phase diagram as the dashed curve. The vertical line drawn on the figure indicates the alloy composition under study. It is evident that the T_0 temperature of the alloy is 1300 °C (1573 K). The phase fields at lower temperatures are not shown to clearly depict T_0 curve. Figure 6 indicates that the temperature the solid (both regions A and B) reaches is much higher than that of the liquidus

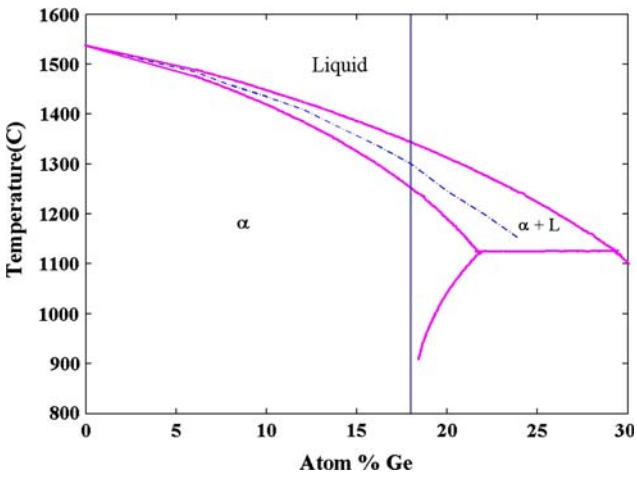

Fig. 7—Fe-rich portion of the Fe-Ge phase diagram showing the T_0 curve. The blue line indicates the composition of the alloy.

temperature (T_l) during rapid laser heating. Solidus (T_s) and liquidus (T_l) temperatures are indicated on the figure. The calculated heating rate is found to be very high (10^4 K/s). Therefore, it is likely that the solid will be thermally superheated sufficiently high so that its temperature will reach T_0 prior to melting during rapid heating of the sample. Therefore, the minimum degree of superheating required is 50 °C. An approximate value of the degree of superheating can be obtained using the results of computer simulation. The temperature at which the first liquid is found to form during computer simulation can be treated as the temperature to which the solid has been superheated as compared to the solidus temperature. The simulation results indicate that the superheating is 57 °C. After the solid temperature reaches T_0 during high rates of heating, growth of the liquid into the solid no longer requires adjustment of solid and liquid composition, and the supersaturated alloy then melts in a partitionless manner. Once melting occurs, the liquid is undercooled due to rapid cooling (10^4 K/s). During subsequent solidification, segregation is not constrained. Therefore, this will facilitate separation into the liquid and solid regions of different compositions. The formation of region A in the present case can be visualized in this manner.

We will now discuss the microstructural evolution in layer B. The microstructural evolution during the process of laser resolidification is controlled by growth kinetics.[2] The selection of the phases and morphology during solidification depends on alloy composition and solidification conditions such as growth velocity and temperature gradient. It has been argued that, in a given growth environment, the stability of one phase or morphology is determined by its solid/liquid interface temperature under constrained growth conditions under a positive temperature gradient.[2,11] The phase or morphology growing at the highest interface temperature is chosen as the one expected to grow under the condition of abundant nucleation of all phases. The solid/liquid interface temperature of any phase or morphology is calculated as a function of interface velocity at a particular temperature gradient. This function is called the interface response function.[22] To obtain a better insight into the growth mechanism, the same analysis as used by Kurz *et al.*[11] has been applied here.

Therefore, the prediction of the most stable (thermodynamically and kinetically) phase and growth morphology requires the determination of the interface response functions of all possible phases and growth morphologies for a given alloy composition in a given growth condition. In the present case, the relevant phases are α_2 (B2) and α(bcc) and growth morphologies are plane front, cells/dendrite. For cellular growth, we have adopted the model by Burden and Hunt.[23–25]

The growth temperature of a single-phase plane front without solute drag and assuming linear attachment kinetics is given by[23]

$$T_P = T_f + C_l^* m_V - \left(R_g T_f^2/\Delta H_f\right)\left(\frac{V}{V_0}\right) \qquad [3]$$

where T_f is the melting temperature of the pure component, C_l^* the composition of liquid at the interface, R_g the universal gas constant, ΔH_f the molar heat of fusion, and V_0 a kinetic parameter. Under steady-state condition, $C_l^* = C_0/k$, where C_0 is the alloy composition and k is the velocity-dependent partition coefficient. For collision-limited growth, *e.g.*, in the case of α phase, V_0 is taken as the velocity of sound in the melt. The term V_0 is replaced by diffusive speed, V_d in the case of the diffusion-limited growth, which is the case for growth of α_2 phase. According to Eq. [3], the interface temperature of the α-phase plane front will always be higher than that of the α_2-phase plane front provided other thermophysical parameters remain the same. Therefore, the α-phase plane front will have a growth advantage as compared to the α_2 phase plane front. In subsequent calculations, we will consider the case of the α-phase plane front temperature only.

The cellular/dendritic growth is modelled by the Kurz–Giovenella–Trivedi (KGT) model[24] modified by Burden and Hunt.[25] The KGT model is based on the Ivantsov solution of a parabolic needle crystal.[26] According to this model, the radius of the cell/dendrite tip (R) is given by the smallest root of the quadratic equation:

$$\frac{M}{R^2} + \frac{N}{R} + G = 0 \qquad [4]$$

where

$$M = 4.\pi^2 \cdot \Omega$$

$$N = \frac{2 \cdot m \cdot C_0 \cdot P(1-k)\xi_C}{1 - (1-k)\cdot \mathrm{Iv}(P)}$$

in which G is the thermal gradient, Ω the Gibbs–Thomson coefficient (ratio of surface energy to volumetric entropy of fusion), C_0 the alloy composition, m the velocity-dependent slope of the liquidus, and k the velocity-dependent partition coefficient. The stability function, ξ_C, is given by

$$\varepsilon_C = 1 + \frac{2k}{1 - 2k - \left\{1 + \left[\left(2\pi/\mathrm{P_C}\right)^2\right]\right\}^{1/2}} \qquad [5]$$

where P_C is the Pèclet number ($P_C = VR/2D$) and D is the solute diffusivity in liquid.

The value of temperature gradient, G, has been determined from heat-transfer calculation and has been taken as 10^4 K/cm[12] for all relevant growth conditions. The velocity-dependent partition coefficient and liquidus slope are given by**

$$k = (k_e + V/V_D)/(1 + V/V_D)$$

$$m = m_0\left(1 - \frac{1 + (k_e - k(1 - \log(k/k_e)))/(1 - k_e)}{1 - (1-k)\mathrm{Iv}(P)}\right)$$

where k_e is the equilibrium partition coefficient and V_D is the interface diffusive velocity.[27] Using thermophysical parameters (as given in Table II), Eq. [8] is solved numerically to obtain a unique solution of R as a function of V.

The cell tip temperature is given by[25]

$$T_d = T_l - \frac{2\Gamma}{R} + C_l^* m_V - \left(R_g T_l^2/\Delta H_f\right)\left(\frac{V}{V_0}\right) - \frac{GD}{V} \qquad [6]$$

Table II. Values of Thermophysical Properties Used for Calculation

Symbol	Parameters	Values
T_M	melting point of pure iron (K)	1812
Ω	Gibbs–Thomson coefficient (K·m)	1.53×10^{-7}[15]
V_s	velocity of sound (ms^{-1})	2000
V_d	diffusive speed (ms^{-1})	15[18]
C_0	alloy composition (at. pct)	18
m_l	equation liquidus slope (K/at. pct)	–14.78
k_0	equation partition coefficient (no unit)	0.78856
μ ($= RT_M^2/L$)	kinetic coefficient (K)	1150[15]
L	molar heat of fusion (J/mol)	19,090
R_g	universal gas constant (J/mol·K)	8.3146
G	thermal gradient (K/cm)	10^4
γ	solid-liquid interfacial energy (J/m^3)	0.348[29]
D	diffusivity in the liquid (m^2/s)	5×10^{-9}[18]

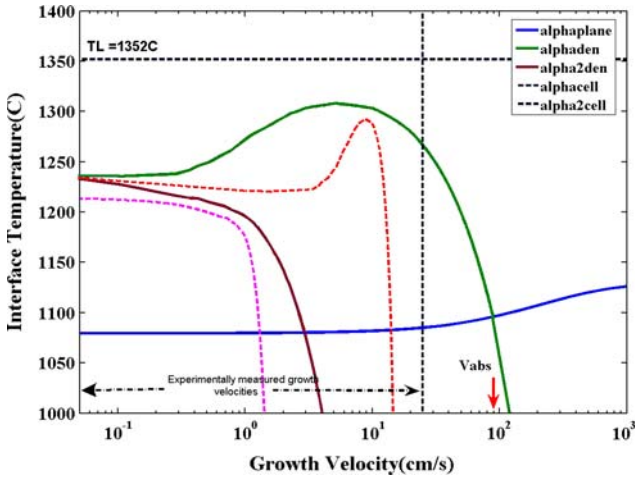

Fig. 8—Calculated interface temperature *vs* growth velocity of different phases and growth morphologies. T_l indicates the liquidus temperature of the alloy.

**Efforts are made to apply the expression of the velocity-dependent partition coefficient given by Aziz and Kaplan,[28] and the interface temperatures (T_i) of the respective phases have determined as a function of growth velocity. The difference in the T_i value is about 3.5 pct from the values reported here.

where C_l^* is the composition of the liquid at the dendrite tip,

$$C_l^* = \frac{C_0}{1-(1-k)\mathrm{Iv}(P)} \quad [7]$$

which is obtained from the numerical solution of the KGT equation;[24] V_0, the kinetic parameter, and the other parameters were defined earlier.

As already discussed, V_0 is taken as the velocity of sound in the melt for the α phase and as diffusive speed for the α_2 phase. The last term in Eq. [5] is due to undercooling in the cellular regime. For dendritic growth, this term goes to zero.

Equations [3] through [6] are solved numerically to obtain the interface temperatures of different growth morphologies. The interface temperatures of different phases and growth morphologies are plotted in Figure 8 as a function of the growth velocities. The range of velocities attained during solidification has been marked in the figure. It is clear that the α-FeGe phase can grow with the highest interface temperature in the velocity range observed during directional solidification. The experimental results also indicate the formation of α-FeGe dendrites in the B layer of the resolidified zone. Therefore, the formation of α-FeGe dendrites can be rationalized in the B layer.

V. CONCLUSIONS

1. The laser resolidification of Fe-18 at. pct Ge alloy leads to the growth of dendrite morphology in the resolidified layer.
2. A two-layer (A and B) microstructure could be observed at lower laser scanning rates. The A layer is suggested to form due to partitionless melting during rapid laser heating followed by solidification of the undercooled melt, which is not constrained to partitioning.
3. The microstructural evolution of the B layer can be quantitatively explained using the cell/dendrite growth models for directional solidification. The formation of α-phase dendrite has been suggested.

ACKNOWLEDGMENTS

The authors would like to acknowledge the (CSIR) and Department of Science and Technology (DST), Govt. of India for funding and Dr. Rolf Galun, Caterpillar Inc. for laser processing of samples.

REFERENCES

1. J. Singh: *J. Mater. Sci.*, 1994, vol. 29, pp. 5232–58.
2. M. Gremaud, M. Carrard, and W. Kurz: *Acta Metall. Mater.*, 1991, vol. 39 (7), pp. 1431–43.
3. G. Sepold and R. Becker: in *Science and Technology of Undercooled Melts*, R. Sahm, H. Jones, and C.M. Adams, eds., NATO ASI Series, Martinus Nijhoff, Dordrecht, Germany, 1985, p. 112.
4. U.K. Mudali and R.K. Dayal: *J. Mater. Eng. Perf.*, 1992, vol. 1 (3), pp. 341–45.
5. K. Biswas, G. Phanikumar, D.M. Herlach, and K. Chattopadhyay: *Mater. Sci. Eng. A*, 2007, vols. 449–451, pp. 12–17.
6. S. Yang, W.D. Huang, X. Lin, Y.P. Su, and Y.H. Zhou: *Scripta Mater.*, 2000, vol. 42, pp. 543–48.
7. S.C. Gill, M. Zimmermann, and W. Kurz: *Acta Metall. Mater.*, 1992, vol. 40 (11), pp. 2895–2906.
8. K. Chattoadhyay, V.T. Swamy, and S.L. Agarwala: *Acta Metall.*, 1990, vol. 38, pp. 521–31.
9. G. Phanikumar, P. Dutta, R. Galun, and K. Chattopadhyay: *Mater. Sci. Eng. A*, 2004, vol. 371, pp. 91–102.
10. A. Pramanick, S. Chatterjee, V. Bhattacharya, and K. Chattopadhyay: *J. Mater. Res.*, 2005, vol. 20, pp. 1580–89.
11. M. Rappaz, B. Carrupt, M. Zimmerman, and W. Kurz: *Helv. Phys. Acta*, 1987, vol. 60, pp. 924–36.
12. S. Sarkar, P. Mohan Raj, S. Chakraborty, G. Phanikumar, K. Chattopadhyay, and P. Dutta: *J. Mater. Sci.*, 2003, vol. 38, pp. 155–64.
13. S. Bysakh, S.K. Mitra, G. Phanikumar, J. Majumdar, and K. Chattopadhyay: *Metall. Mater. Trans. A*, 2003, vol. 34A, pp. 2621–31.
14. T.B. Massalski: *Binary Alloy Phase Diagrams*, ASM, Metals Park, OH, 1990.
15. K. Biswas, G. Phanikumar, D. Holland-Moritz, D.M. Herlach, and K. Chattopadhyay: *Phil. Mag.*, 2007, vol. 87, pp. 3817–37.
16. W.P. Allen, H.J. Fecht, and J.H. Perepezko: *Scripta Metall.*, 1989, vol. 23, pp. 643–46.
17. E. Gamsjäger, J. Svoboda, F.D. Fischer, and M. Rettenmayr: *Acta Mater.*, 2007, vol. 55, pp. 2599–2607.
18. M.J. Aziz: *J. Appl. Phys.*, 1982, vol. 53, pp. 1158–68.
19. E.A. Brandes: *Smithells Metals Reference Handbook*, 6th ed., Butterworth, London, 1983.
20. D.S. Kanibolorsky, O.A. Bieloborodova, N.V. Kotava, and V.V. Linsyak: *J. Thermal Anal. Calorim.*, 2003, vol. 73, pp. 583–91.
21. G. Inden and W. Pitch: *Z. Metallkd.*, 1972, vol. 63, pp. 253–56.
22. J. Baker and J. Cahn: in *Selected Works of John Cahn*, W.C. Carter and W.C. Johnson, eds., TMS, Warrendale, PA, 1998, pp. 253–88.
23. W.J. Boettinger and S.R. Coriell: in *Science and Technology of Undercooled Melt*, NATO ASI Series, E-No114, P.R. Sahm, H. Jones, and C.M. Adams, eds., Martinus Nijhoff, Dordrecht, 1986, p. 81.
24. W. Kurz, B. Giovanola, and R. Trivedi: *Acta Metall.*, 1986, vol. 34, pp. 823–30.
25. M. Burden and J.D. Hunt: *J. Cryst. Growth*, 1974, vol. 22, pp. 109–16.
26. G.P. Ivanstov: *Dokl. Akad. Nauk SSSR*, 1947, vol. 58, pp. 567–69.
27. W. Kurz and D.J. Fisher: *Acta Metall.*, 1981, vol. 29, pp. 11–20.
28. M.J. Aziz and T. Kaplan: *Acta Metall.*, 1988, vol. 36, pp. 2335–47.
29. F. Spaepen and R.B. Meyer: *Scripta Metall.*, 1976, vol. 10, pp. 257–63.